ACS APPLIED MATERIALS & INTERFACES

Research Article

www.acsami.org

Effective Suppression of Dendritic Lithium Growth Using an Ultrathin Coating of Nitrogen and Sulfur Codoped Graphene Nanosheets on Polymer Separator for Lithium Metal Batteries

Won-Kyung Shin, Aravindaraj G. Kannan, and Dong-Won Kim*

Department of Chemical Engineering, Hanyang University, Seoul 133-791, Korea

Supporting Information

ABSTRACT: The enhanced stability of lithium metal is vital to the development of high energy density lithium batteries due to its higher specific capacity and low redox potential. Herein, we demonstrate that nitrogen and sulfur codoped graphene (NSG) nanosheets coated on a polyethylene separator stabilized the lithium electrode in lithium metal batteries by effectively suppressing dendrite growth and maintaining a uniform ionic flux on the metal surface. The ultrathin layer of NSG nanosheets also improved the dimensional stability of the polymer separator at elevated temperatures. In addition, the enhanced interfacial interaction between the NSG-coated separator and lithium metal via electrostatic attraction released the surface tension of lithium metal and suppressed the initiation of dendrite growth on lithium metal. As a result, the electrochemical performance of a lithium metal cell composed of a $LiNi_{0.8}Co_{0.15}Al_{0.05}O_2$ positive electrode with an NSG-coated separator was remarkably improved as compared to the cell with an uncoated polyethylene separator.

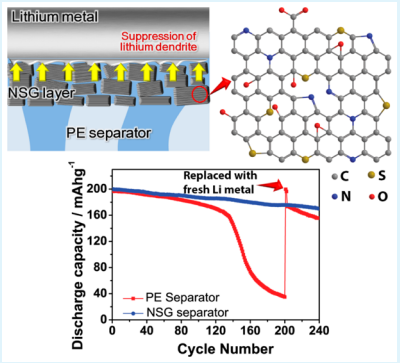

KEYWORDS: *doped graphene, ultrathin coating, coated separator, lithium dendrite, lithium metal battery*

INTRODUCTION

The advent of electric vehicles and other high energy density applications has intensified the research efforts on lithium metal-based batteries, as metallic lithium can provide a high specific capacity (~3862 mAh g^{-1}), enabling it as a promising negative electrode for next-generation battery systems including lithium−sulfur and lithium−air batteries.[1−8] These batteries offer 3−5 times higher theoretical energy density than the currently available battery chemistries. However, the instability of lithium electrodes is one of the greatest challenges hindering the successful development of lithium metal batteries. Lithium metal is unstable against nearly all chemical species and reacts with organic solvents and salts in liquid electrolytes. Moreover, continuous deposition and stripping of lithium may induce uncontrollable dendritic Li growth, which, in turn, leads to internal short circuits, failure, and eventually explosions.[9−11] Recently, Yang et al. reported that a 3D current collector with a submicron skeleton and high active surface area could significantly improve the electrochemical deposition behavior of lithium.[12] When using a planar current collector, spatial confinement of Li metal plating/striping is absent, resulting in the formation of various morphologies (e.g., mossy and dendritic structures) on the lithium electrode. Numerous strategies have been adopted to overcome these problems, such as the utilization of stable solid electrolyte interphase (SEI) forming additives,[13−15] protective coating layers on the lithium metal,[16−18] and use of polymer electrolytes.[19−21] Composite polymer separators with inert ceramic particles have also been explored to mechanically inhibit dendritic growth.[22−24] Ryou et al. reported that mussel-inspired polydopamine-coated separators effectively suppressed lithium dendrite growth by facilitating both a homogeneous ionic flux distribution on the lithium metal surface and strong catecholic adhesion of the separator on the lithium electrode.[25,26] More recently, Yan et al. demonstrated that ultrathin 2-D hexagonal boron nitride and graphene prepared via chemical vapor deposition could effectively act as stable interfacial layers due to their remarkable stability, mechanical strength, and flexibility.[27] In our work, we demonstrate that an ultrathin nitrogen and sulfur codoped graphene (NSG) layer deposited on a polyethylene (PE) separator by a simple vacuum infiltration method effectively suppressed the dendritic growth of lithium metal, as illustrated in Figure 1. The NSG coating layer is very thin as compared to other ceramic coatings in micrometer scales, which can provide higher energy density of the cell with the NSG separator. The incorporation of heteroatom dopants could induce structural deformations due to local strains induced in the carbon framework,[28,29] thereby allowing for easy ionic migration while maintaining a uniform ionic flux on the Li metal surface. This is in contrast to the characteristics of a PE separator, where a microporous morphology leads to dendritic growth in close proximity to porous structures.[30] Moreover, the lone pair electrons in the heteroatom dopants (N and S) led to the generation of negative charge, resulting in enhanced interfacial

Received: August 20, 2015
Accepted: October 13, 2015
Published: October 13, 2015

DOI: 10.1021/acsami.5b07730
ACS Appl. Mater. Interfaces 2015, 7, 23700−23707

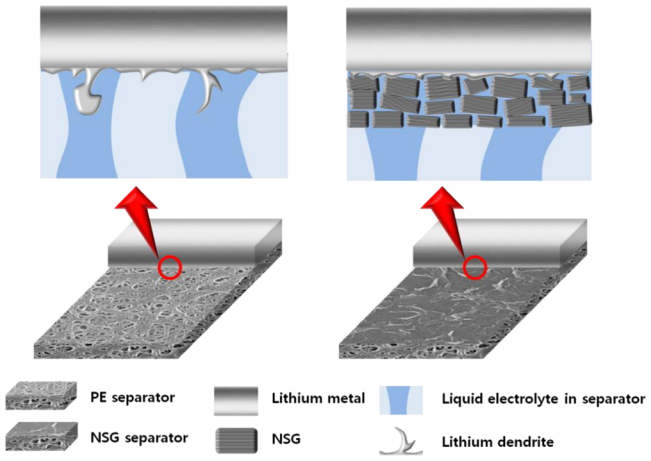

Figure 1. Schematic illustration of dendrite growth on the lithium metal electrode with the PE separator (left) and NSG-coated PE separator (right).

interactions between the NSG-coated separator and the lithium electrode. The NSG coating also imparted thermal stability to the PE separator, thus preventing thermal shrinkage of the separator at elevated temperature and enhancing battery safety. The cycling performance of the lithium metal cell employing an NSG-coated separator was remarkably improved as compared to the cell with a pristine PE separator.

EXPERIMENTAL SECTION

Synthesis of N,S-Codoped Graphene and Surface Modification of the PE Separator. The N,S-codoped graphene (NSG) was synthesized as described in our earlier work.[31,32] In a typical synthesis procedure, 900 mg of thiourea was added to 70 mL of DI water containing 300 mg of graphene oxide (GO), and the solution was subsequently stirred for 4 h. The reaction mixture was then transferred to a Teflon-lined stainless steel autoclave and heated at 180 °C for 12 h, at which point the autoclave was allowed to cool down naturally. The resulting product was alternatively washed with ethanol and DI water, and then vacuum-dried at room temperature. To prepare the NSG-coated separator, NSG (0.005 wt %) was first dispersed in ethanol by sonication for 4 h. The solution was then applied on a PE separator (ND 420, Asahi) by a simple vacuum infiltration method. Finally, the NSG separator was dried in a vacuum oven at 80 °C for 24 h and subsequently used for characterization and performance evaluation. A GO-coated separator was also prepared as a control sample according to the same procedure, with NSG being replaced by GO.

Electrode Preparation and Cell Assembly. The positive electrode was prepared by coating an *N*-methyl-2-pyrrolidone (NMP)-based slurry containing 85.0 wt % $LiNi_{0.8}Co_{0.15}Al_{0.05}O_2$ (Ecopro Co. Ltd.), 7.5 wt % poly(vinylidene fluoride) (PVdF), and 7.5 wt % super-P carbon (MMM Co.) onto an aluminum foil. The active mass loading in the positive electrode corresponded to a capacity of approximately 2.0 mAh cm^{-2}. The negative electrode consisted of a 100 μm thick lithium foil (Honjo Metal Co. Ltd.) pressed onto a copper current collector. The mass loading in the negative electrode was about 4.48 mg cm^{-2}, corresponding to 17.3 mAh cm^{-2}. A CR2032-type coin cell was assembled by sandwiching the separator between the lithium negative electrode and the $LiNi_{0.8}Co_{0.15}Al_{0.05}O_2$ positive electrode. The cell was then injected with an electrolyte solution consisting of 1.15 M $LiPF_6$ in ethylene

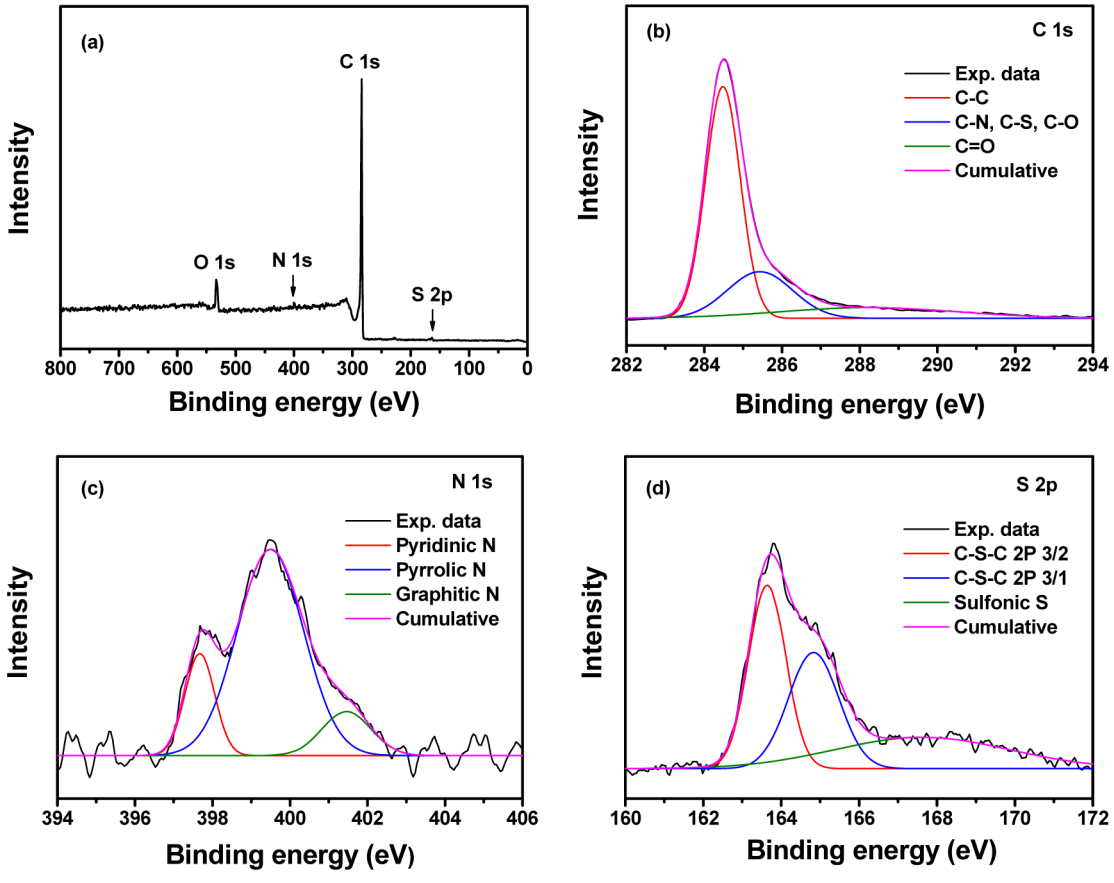

Figure 2. (a) XPS survey. (b) C 1s, (c) N 1s, and (d) S 2p spectra of the NSG separator.

DOI: 10.1021/acsami.5b07730
ACS Appl. Mater. Interfaces 2015, 7, 23700−23707

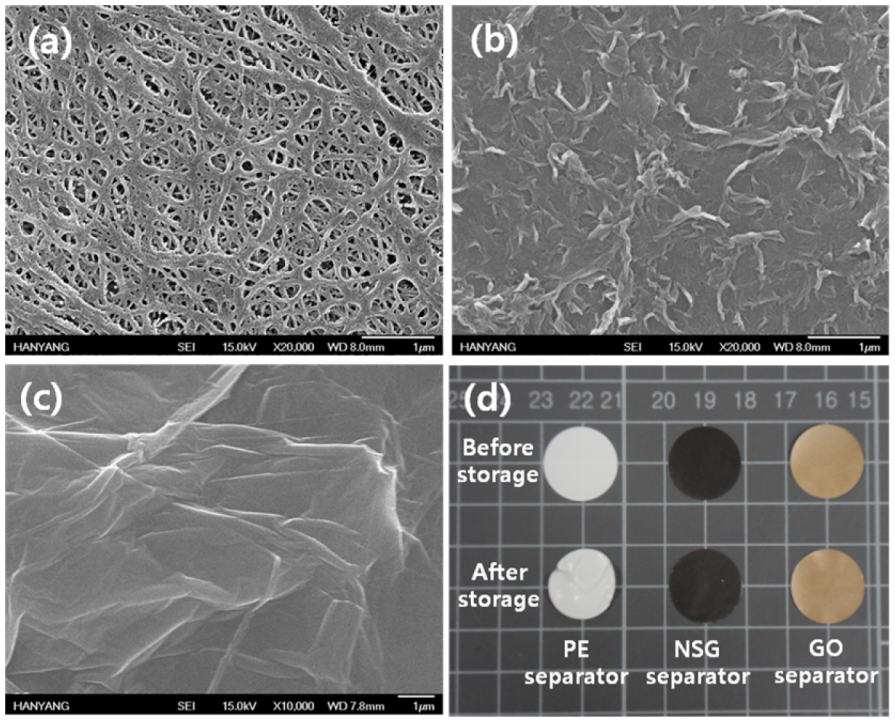

Figure 3. SEM images of the surface of the (a) PE separator, (b) NSG separator, and (c) GO separator. (d) Photographs of the PE, NSG, and GO separators after storage at 130 °C for 1 h.

carbonate/diethyl carbonate (3/7 by volume, battery grade, PANAX ETEC Co. Ltd.). All cells were assembled in a drybox filled with argon gas.

Measurements. The amount of doping and the nature of chemical changes caused by N,S-codoping were analyzed using X-ray photoelectron spectroscopy (XPS, VG multilab ESCA system, 220i). The NSG-coated separator was further characterized using Raman spectroscopy (Dongwoo Optron, MonoRa 780i) to investigate its structure and graphene quality. The morphologies of the PE, GO-coated, and NSG-coated separators were examined via field emission scanning electron microscopy (FE-SEM, JEOL JSM-6330F). The separator wettability was investigated by contact angle measurements with a water droplet, using a contact angle analyzer (Surfacetech Co., Ltd., GS). The thermal shrinkage of the separators was measured in terms of their dimensional changes after being held at 130 °C for 1 h. The separator soaked in a liquid electrolyte was sandwiched between two stainless steel electrodes for conductivity measurements. AC impedance measurements were performed to measure ionic conductivity and interfacial resistances using a Zahner Electrik IM6 impedance analyzer over a frequency range of 1 mHz to 100 kHz with an amplitude of 10 mV. Charge and discharge cycling tests of the Li/$LiNi_{0.8}Co_{0.15}Al_{0.05}O_2$ cells were performed at a current density of 1.0 mA cm^{-2} (0.5C rate) over a voltage range of 2.6−4.3 V using battery test equipment (WBCS 3000, WonA Tech Co., Ltd.). Surface morphologies of the lithium electrodes in the cells were analyzed by FE-SEM after repeated cycling. The lithium electrode was washed several times in anhydrous dimethyl carbonate to remove residual electrolyte, followed by vacuum drying overnight at room temperature. In order to investigate the interfacial interaction between the lithium electrode and the separator, shear strength was evaluated using a universal testing machine (Instron 5966). Stress−strain measurements were carried out with a load cell of 10 N mm min^{-1} using the sample dimensions of 20 mm × 100 mm (width and length).

RESULTS AND DISCUSSION

NSG was prepared from graphene oxide and thiourea by a simple hydrothermal method. Successful doping with nitrogen and sulfur heteroatoms as well as a simultaneous reduction of oxygen functional groups were confirmed by XPS spectra, as depicted in Figure 2. The survey spectrum in Figure 2a shows the presence of carbon, oxygen, nitrogen, and sulfur elements. The amount of nitrogen and sulfur doping in the NSG was calculated to be 1.9 and 2.5 at %, respectively. The C/O ratio was calculated to be 1.91 and 9.75 for GO and NSG, respectively. Such a high C/O ratio for the NSG sample demonstrates that the oxygen functional groups in GO have been highly reduced during the hydrothermal process. The C 1s peak could be resolved into three peaks at 284.5, 285.4, and 288.2 eV, indicating the presence of carbon with different bonding configurations.[33] The peak at 284.5 eV is attributed to graphitic carbon, whereas the peak at 285.4 eV corresponds to C-O, C-N, and C-S groups. The third peak at a higher binding energy indicates the presence of residual carbonyl and carboxyl groups in the NSG nanosheets. The N 1s peak could also be resolved into three peaks at 397.7, 399.5, and 401.3 eV, which correspond to pyridinic, pyrrolic, and graphitic N, respectively.[34] Such results confirm that nitrogen was successfully incorporated into the carbon framework with different configurations. The S 2p peak could also be deconvoluted into three peaks; the peaks at lower binding energies (163.6 and 164.8 eV) correspond to sulfur atoms bound in aromatic carbon structures, while the third broad peak at a higher binding energy is associated with sulfur in C-SO_x states.[35] On the basis of these findings, the structure of NSG nanosheets was derived as shown in Figure S1. The NSG separator was further characterized by Raman spectroscopy (Figure S2). GO shows the presence of D- and G-bands around 1355 and 1600 cm^{-1}, respectively.[36] In contrast, the G-bands arising from graphitic carbon in NSG and the NSG separator are red-shifted to 1587 cm^{-1}, indicating *n*-type substitutional doping of the graphene.[37] The D-band observed at 1355 cm^{-1} in NSG was red-shifted to 1347 cm^{-1} in the NSG separator. In addition, the intensity of the D-band in the NSG separator is much higher than that of

DOI: 10.1021/acsami.5b07730
ACS Appl. Mater. Interfaces 2015, 7, 23700−23707

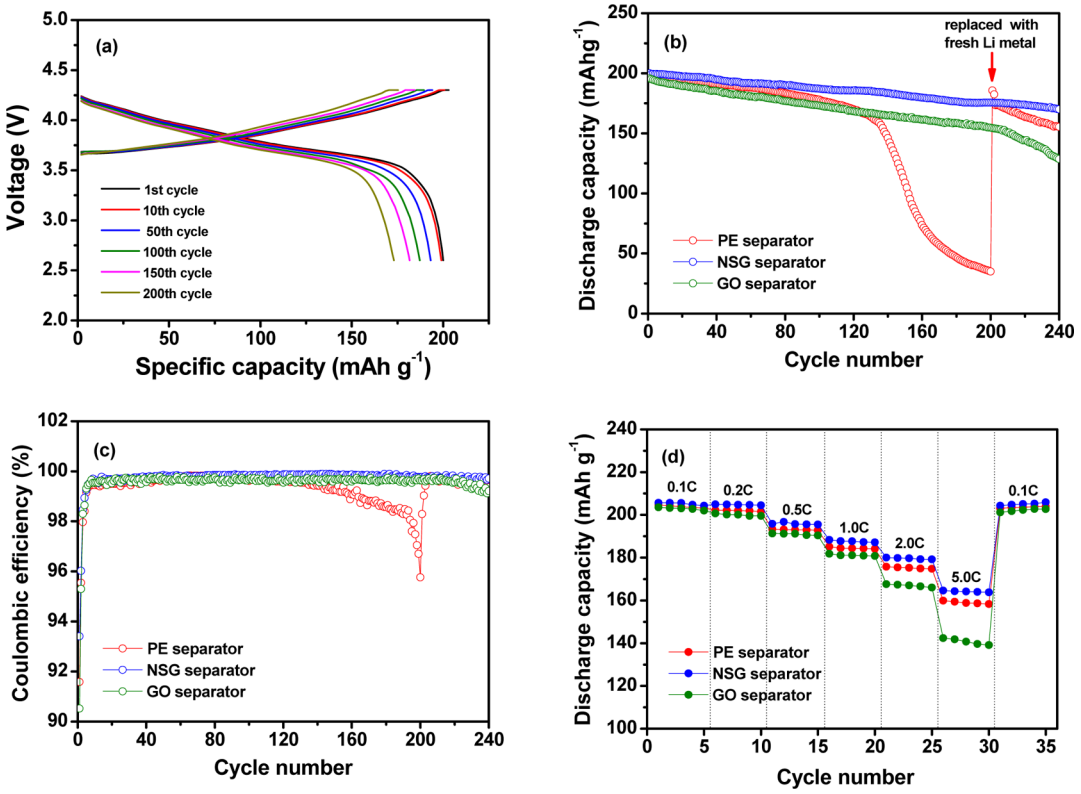

Figure 4. (a) Charge and discharge curves of the Li/$LiNi_{0.8}Co_{0.15}Al_{0.05}O_2$ cell prepared with the NSG separator at 0.5C rate. (b) Discharge capacities and (c) Coulombic efficiencies of the Li/$LiNi_{0.8}Co_{0.15}Al_{0.05}O_2$ cells assembled with different separators as a function of the cycle number. (d) Rate capability of the Li/$LiNi_{0.8}Co_{0.15}Al_{0.05}O_2$ cells assembled with different separators.

the other samples. The higher intensity and red shift are attributed to the presence of an additional peak from the CH_2 twist in the PE separator, which is more dominant than the D-band intensity.[38] An additional minor peak at 1133 cm^{-1} in the spectrum of the NSG separator is attributed to C−C stretching arising from the PE separator. Moreover, the appearance of a broad 2D band at 2700 cm^{-1} in the NSG and NSG separator spectra indicates the presence of both single- and few-layer graphene nanosheets.[39] Finally, an additional broad peak in the range of 2850−2950 cm^{-1} is attributed to the presence of aliphatic chains in the PE separator. These results confirm that NSG was successfully deposited onto the PE separator.

The morphologies of the PE separator, NSG-coated PE separator (NSG separator), and GO-coated PE separator (GO separator) were compared by SEM analyses. The surface of a pristine PE separator (Figure 3a) exhibited a uniformly interconnected submicron porous structure. On the other hand, the surface of the NSG separator showed a homogeneous morphology with uniform surface coverage by NSG nanosheets (Figure 3b). Furthermore, the NSG nanosheets were strongly adhered to the surface of the PE separator without any agglomeration. The two-dimensional structure of NSG allowed it to be deposited only on the surface without permeating into the separator. In this work, NSG was coated on only one side of the separator to prevent short circuits that may arise due to the conductive nature of the NSG nanosheets. The thickness of the NSG coating layer was measured to be 60 nm, as shown in the cross-sectional SEM image (Figure S3). The random arrangement of 2-D graphene nanosheets is known to increase the tortuosity of ionic movement. However, the NSG separator showed only a slight reduction in ionic conductivity (3.6×10^{-4} S cm^{-1}) when compared to that of a pristine PE separator (4.2×10^{-4} S cm^{-1}). GO, which was employed as a control sample, forms a dense and stiff film on the PE separator (Figure 3c), leading to an ionic conductivity (2.0×10^{-4} S cm^{-1}) that is roughly half the value obtained with the pristine PE separator. These results indicate that the formation of a mesoporous NSG morphology (as demonstrated in our previous report[31]), along with line and point defects present in the carbon framework, facilitates ionic movement.[40] In addition, the structural deformations induced by heteroatom doping could enhance lithium ion transport. As evident in Figure S4, surface modification of the PE separator with NSG does not significantly affect the wettability of the structure. The high contact angle for the NSG separator arises from the significant reduction of GO, as evident from the high C/O ratio of 9.75 for the NSG sample, as previously explained. Such a significant reduction is attributed to the use of thiourea as a source of nitrogen and sulfur dopants to prepare NSG in the hydrothermal process, which simultaneously acts as a reducing agent as well. On the other hand, the contact angle on the GO separator was relatively low (50.8°), which can be ascribed to the presence of oxygen functional groups in the GO coating layer. In order to investigate the effect of NSG or GO coatings on the thermal stability of a PE separator, thermal shrinkage was measured after storing the separator at 130 °C for 1 h, as shown in Figure 3d. The pristine PE separator tended to shrink when exposed to high temperatures. In contrast, the utilization of a thermally stable NSG or GO coating on the PE separator prevented dimensional changes at elevated temperatures. Consequently, NSG and GO provided mechanical reinforcement so as to preserve the mechanical integrity of the separator

DOI: 10.1021/acsami.5b07730
ACS Appl. Mater. Interfaces 2015, 7, 23700−23707

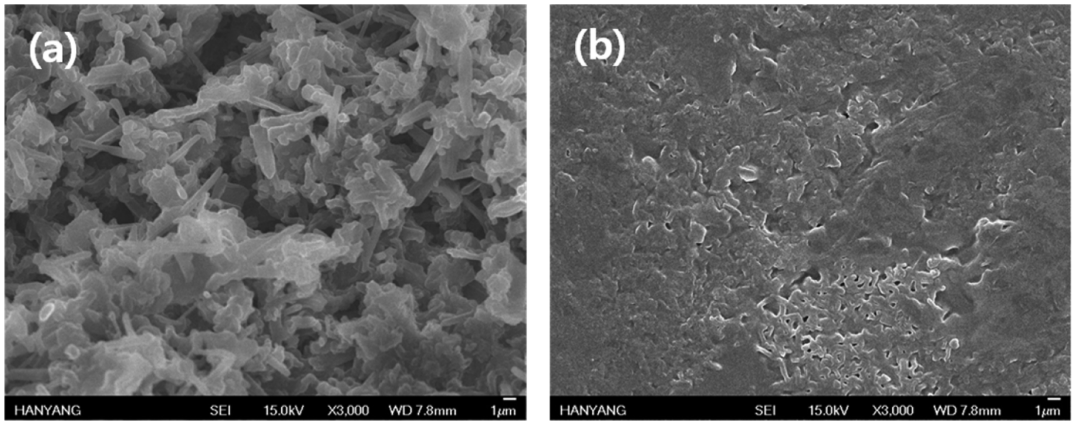

Figure 5. SEM images of lithium electrodes cycled with (a) PE and (b) NSG separators; the images were obtained after 200 cycles at 25 °C.

at high temperatures. The tensile measurements of different separators were also carried out, and the results are given in Figure S5. Clearly, the NSG separator exhibited superior mechanical strength than the pristine PE separator.

The effectiveness of the NSG-coated separator in suppressing dendritic lithium growth was investigated by cycling Li/$LiNi_{0.8}Co_{0.15}Al_{0.05}O_2$ cells with different separators in the same liquid electrolyte (1.15 M $LiPF_6$ in ethylene carbonate/diethyl carbonate, 3/7 by volume) at 0.5C rate. The charge and discharge curves of the cell with the NSG separator are presented in Figure 4a. The specific capacity was calculated based on the weight of the active $LiNi_{0.8}Co_{0.15}Al_{0.05}O_2$ material in the positive electrode. The cell assembled with the NSG separator delivered a high initial discharge capacity of 200.0 mAh g^{-1}. The capacity recovered during constant voltage charging is small, which indicates that the cell has a low internal cell resistance and is thus capable of delivering high capacity. The cell exhibited stable cycling characteristics; that is, it delivered 85.0% of the initial discharge capacity after 240 cycles. Figure 4b shows the discharge capacities of Li/$LiNi_{0.8}Co_{0.15}Al_{0.05}O_2$ cells with different separators. The cell with the PE separator showed an increase in overpotential and a reduction in the reversible capacity with repeated cycling (Figure S6), leading to significant capacity fading after 130 cycles. The capacity decline observed for rechargeable lithium metal batteries is mainly associated with dendrite formation and exhaustion of the liquid electrolyte.[9] The formation of lithium dendrites exposes fresh Li metal surfaces to the electrolyte, and thus, additional SEI layers are continuously generated with gradual consumption of the electrolyte solution. Moreover, lithium dendrites can become isolated from the lithium electrode during repeated cycling. The isolated lithium can then react with the organic electrolyte due to its highly reactive nature, severely degrading the cycling performance. To further substantiate the presumption that the lithium electrode was primarily responsible for cell failure, the cell with pristine PE was disassembled carefully after 200 cycles, reassembled with fresh lithium metal, and replenished with the liquid electrolyte solution. As shown in Figure 4b, the discharge capacity of the reassembled cell fully recovered to its initial value, confirming that the cycling performance of the PE separator cell was significantly affected by the state of the lithium electrode. The rapid capacity decline of the PE cell upon further cycling can be attributed to degradation of the positive electrode. On the other hand, the cell assembled with the NSG separator exhibited a stable cycling performance with no significant capacity fading up to the 240th cycle. Such superior capacity retention can be ascribed to the enhanced stability of the lithium electrode by modification with an NSG layer. Figure 4c shows the Coulombic efficiencies of the Li/$LiNi_{0.8}Co_{0.15}Al_{0.05}O_2$ cells assembled with different separators. The Coulombic efficiencies of the cells at the first cycle are 91.6, 93.4, and 92.1 for PE, NSG, and GO separators, respectively. The irreversible capacity at the first cycle is associated with irreversible reactions of organic solvents at the electrode surface.[41] Thus, the higher Coulombic efficiency in the cell with NSG and GO separators suggests that the coating layer can reduce the reductive decomposition of the organic electrolyte at the lithium electrode. The Coulombic efficiencies steadily increased with cycling and were measured to be 99.6, 99.8 and 99.7% at the 100th cycle for the cells with PE, NSG, and GO separators, respectively. It should be noted that the Coulombic efficiency was decreased after the 120th cycle in the cell with the PE separator. As mentioned earlier, the formation and growth of lithium dendrites exposes fresh Li metal to the electrolyte solution and the additional SEI layers are continuously generated with irreversible reactions of organic solvents at the electrode surface, which leads to a decrease of Coulombic efficiency. The rate performance of the Li/$LiNi_{0.8}Co_{0.15}Al_{0.05}O_2$ cells assembled with different separators is compared in Figure 4d. The discharge capacities of the cell with the NSG separator were higher than those of the PE separator cell. However, the cell assembled with the GO separator delivered low discharge capacities at high current rates, which can be ascribed to high ionic resistance due to the presence of a dense and stiff GO coating layer on the separator.

SEM analysis of the lithium electrodes was performed after 200 cycles. The lithium electrode cycled with the PE separator showed extensive rodlike dendrite formation (Figure 5a). The interfacial overpotential was enhanced at the tip of the dendrites due to its coupling to the local electric field. As a result of the inhomogeneous electric field, the dendrite tips experienced increased deposition rates, which, in turn, promoted rapid dendrite growth. In contrast, the lithium electrode with the NSG separator exhibited rather smooth morphologies without any visible dendrite growth, as shown in Figure 5b. Although the lithium electrode with the GO separator showed less dendritic morphology (Figure S7), the deposition of lithium was not so even as compared to lithium with the NSG separator. These results suggest that the thin NSG layer could effectively suppress dendrite growth by facilitating the formation of a uniform distribution of Li^+ ions

DOI: 10.1021/acsami.5b07730
ACS Appl. Mater. Interfaces 2015, 7, 23700−23707

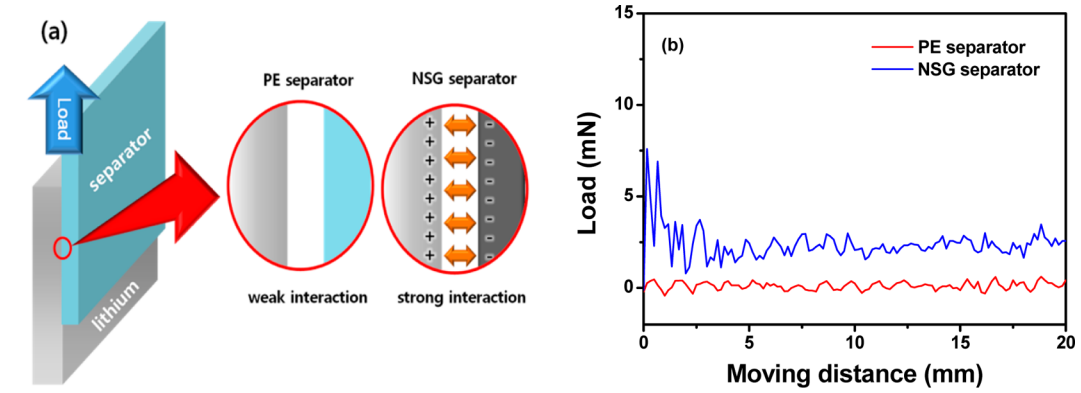

Figure 6. (a) Schematic illustration of shear tests conducted to examine the interfacial interaction between the lithium electrode and separator. (b) Shear force measured between the lithium electrode and the separator.

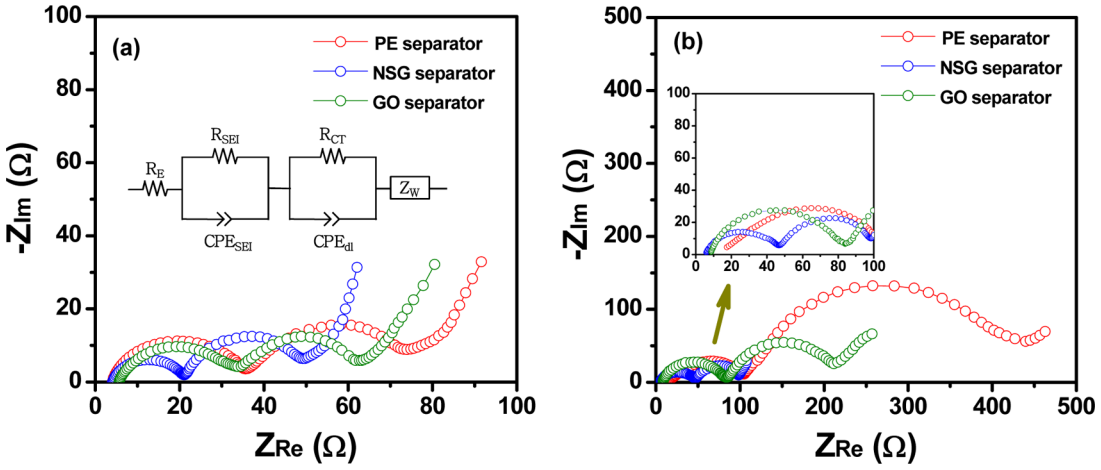

Figure 7. AC impedance spectra of the $Li/LiNi_{0.8}Co_{0.15}Al_{0.05}O_2$ cells assembled with different separators (a) before 200 cycles and (b) after 200 cycles. The equivalent circuit used to fit these spectra is given in the inset in (a), and the inset shown in (b) presents a close-up view in the high frequency range.

over the entire Li surface. In addition, the NSG nanosheets act as physical barriers that inhibit dendrite growth due to their superior mechanical properties.

We postulate that enhanced interfacial interactions between NSG nanosheets and the lithium electrode play a vital role in stabilizing the lithium metal. Unlike the PE separator, NSG nanosheets exhibit a negative charge throughout their surfaces due to lone pair electrons in the heteroatom dopants. Electrostatic attraction between the induced negative charge on the NSG separator and the positively charged lithium metal surface enhances interfacial interactions, as demonstrated in Figure 6a. To validate this postulation, a strip of lithium foil was physically attached to the separator and the force required to slide the separator was measured (Figure 6b). As the PE separator exhibits no interactions with the Li metal electrode, its sliding force is hardly detected. In contrast, the NSG separator with lithium metal required an initial force of 7.6 mN due to electrostatic charge interactions between the Li metal and the NSG coating layer. The force then dropped to 2.0 mN when the separator started sliding. This result confirms that the NSG separator displays strong interfacial interactions with the lithium metal electrode. The enhanced adhesion could release surface tension in the Li metal, thereby suppressing the initiation of dendrite growth on the Li metal surface.[26]

In order to further understand the improvement in the electrochemical performance of the NSG separator-based cell, the AC impedance of the cell was measured. The resulting AC impedance spectra before and after 200 cycles are shown in Figure 7a,b, respectively. Both spectra are composed of two overlapping semicircles in the high and low frequency regions. The semicircle in the high frequency range can be attributed to the resistance of the SEI layer on the electrode (R_{SEI}), while the semicircle in the medium-to-low frequency range is associated with the charge transfer resistance (R_{CT}) between the electrodes and the electrolyte. These spectra could be analyzed using the equivalent circuit given in the inset of Figure 7a. In this circuit, R_E is the electrolyte resistance including electrode contact resistance. R_{SEI} and R_{CT} are the resistance of the SEI film and the charge transfer resistance, respectively. CPE_i (constant phase element) denotes the capacitance of each component to reflect the depressed semicircular shape, and Z_w is Warburg impedance. The values of R_E, R_{SEI}, and R_{CT} deduced from the impedance spectra are summarized in Table 1.

In the cell with the PE separator, the values of R_E, R_{SEI}, and R_{CT} remarkably increased after 200 cycles. The large increase of R_E can be mainly ascribed to exhaustion of the liquid electrolyte due to the deleterious reaction between the electrolyte solution and lithium dendrites isolated from the lithium electrode during repeated cycling, because the isolated lithium can then react with the organic electrolyte due to its highly reactive nature. An increase in interfacial resistances (R_{SEI} and R_{CT}) is related to both growth of the resistive surface layer on the electrodes and

DOI: 10.1021/acsami.5b07730
ACS Appl. Mater. Interfaces 2015, 7, 23700−23707

Table 1. Electrolyte Resistance (R_E), SEI Film Resistance (R_{SEI}), and Charge Transfer Resistance (R_{CT}) of the Li/$LiNi_{0.8}Co_{0.15}Al_{0.05}O_2$ Cells Assembled with Different Separators before and after Cycling

	before cycling			after 200 cycles		
separator	R_E (Ω)	R_{SEI} (Ω)	R_{CT} (Ω)	R_E (Ω)	R_{SEI} (Ω)	R_{CT} (Ω)
PE	4.0	31.7	38.2	14.3	89.4	336.1
NSG	4.1	17.0	28.2	5.8	41.0	51.4
GO	5.6	28.2	27.9	8.5	75.5	127.7

deterioration of the interfacial contacts at electrodes. In the cells with NSG and GO separators, the increase in R_E was not so large as compared to the cell with the PE separator, indicating that the electrolyte loss due to the irreversible reaction was not so significant. Among the cells, the NSG separator cell showed the lowest interfacial resistances after cycling, implying that the cell had a more stable SEI layer that facilitated more efficient lithium ion transfer at the interfaces during cycling. Consequently, an increase in cell impedance was remarkably suppressed in the NSG separator cell, leading to good capacity retention during cycling.

CONCLUSIONS

We demonstrated that a thin NSG layer deposited on a PE separator could effectively stabilize the lithium electrode surface, suppress dendrite formation, and improve the cycling stability of lithium metal batteries. The enhanced performance of the cell with an NSG separator can be attributed to (a) the presence of defects in the NSG layer, which provides a uniform ionic flux on the Li metal surface, (b) the superior mechanical strength of NSG, which acts as a barrier for dendritic growth, and (c) enhanced interfacial interactions between the NSG layer and lithium metal brought about by electrostatic attraction. Finally, the thermally stable NSG layer increased the thermal stability of the PE separator, thereby addressing a critical safety issue associated with lithium metal batteries.

ASSOCIATED CONTENT

Supporting Information

The Supporting Information is available free of charge on the ACS Publications website at DOI: 10.1021/acsami.5b07730.

Chemical structure of the NSG nanosheet; Raman spectra of GO, NSG, and NSG-coated separator; cross-sectional SEM image of the NSG-coated separator; contact angle images; stress−strain curves of different separators; cycling curves of the cell with the PE separator; and SEM image of lithium electrode cycled with GO separator (PDF)

AUTHOR INFORMATION

Corresponding Author

*E-mail: dongwonkim@hanyang.ac.kr.

Notes

The authors declare no competing financial interest.

ACKNOWLEDGMENTS

This work was supported by the Basic Science Research Program of the National Research Foundation of Korea (NRF), funded by the Ministry of Science, ICT, and Future Planning (2014R1A2A2A01002154). Additional support was provided by the R&D Convergence Program of the National Research Council of Science & Technology (NST) of the Republic of Korea.

REFERENCES

(1) Tarascon, J.-M.; Armand, M. Issues and Challenges Facing Rechargeable Lithium Batteries. *Nature* **2001**, *414*, 359−367.
(2) Bruce, P. G.; Freunberger, S. A.; Hardwick, L. J.; Tarascon, J.-M. Li-O_2 and Li-S Batteries with High Energy Storage. *Nat. Mater.* **2012**, *11*, 19−29.
(3) Peng, Z.; Freunberger, S. A.; Chen, Y.; Bruce, P. G. A Reversible and Higher-Rate Li-O_2 Battery. *Science* **2012**, *337*, 563−566.
(4) Xu, W.; Wang, J.; Ding, F.; Chen, X.; Nasybulin, E.; Zhang, Y.; Zhang, J. G. Lithium Metal Anodes for Rechargeable Batteries. *Energy Environ. Sci.* **2014**, *7*, 513−537.
(5) Manthiram, A.; Fu, Y.; Chung, S. H.; Zu, C.; Su, Y. S. Rechargeable Lithium-Sulfur Batteries. *Chem. Rev.* **2014**, *114*, 11751−11787.
(6) Lu, J.; Li, L.; Park, J. B.; Sun, Y. K.; Wu, F.; Amine, K. Aprotic and Aqueous Li-O_2 Batteries. *Chem. Rev.* **2014**, *114*, 5611−5640.
(7) Yin, Y.-X.; Xin, S.; Guo, Y.-G.; Wan, L.-J. Lithium−Sulfur Batteries: Electrochemistry, Materials, and Prospects. *Angew. Chem., Int. Ed.* **2013**, *52*, 13186−13200.
(8) Yang, C.-P.; Yin, Y.-X.; Guo, Y.-G.; Wan, L.-J. Electrochemical (De)Lithiation of 1D Sulfur Chains in Li−S Batteries: A Model System Study. *J. Am. Chem. Soc.* **2015**, *137*, 2215−2218.
(9) Aurbach, D.; Zinigrad, E.; Cohen, Y.; Teller, H. A Short Review of Failure Mechanisms of Lithium Metal and Lithiated Graphite Anodes in Liquid Electrolyte Solutions. *Solid State Ionics* **2002**, *148*, 405−416.
(10) Kim, H.; Jeong, G.; Kim, Y. U.; Kim, J. H.; Park, C. M.; Sohn, H. J. Metallic Anodes for Next Generation Secondary Batteries. *Chem. Soc. Rev.* **2013**, *42*, 9011−9034.
(11) Li, Z.; Huang, J.; Yann Liaw, B.; Metzler, V.; Zhang, J. A Review of Lithium Deposition in Lithium-Ion and Lithium Metal Secondary Batteries. *J. Power Sources* **2014**, *254*, 168−182.
(12) Yang, C.-P.; Yin, Y. -X; Zhang, S.-F.; Li, N.-W.; Guo, Y.-G. Accommodating Lithium into 3D Current Collectors with a Submicron Skeleton Towards Long-life Lithium Metal Anodes. *Nat. Commun.* **2015**, *6*, 8058.
(13) Ota, H.; Shima, K.; Ue, M.; Yamaki, J. I. Effect of Vinylene Carbonate as Additive to Electrolyte for Lithium Metal Anode. *Electrochim. Acta* **2004**, *49*, 565−572.
(14) Jeong, J.; Lee, J.-N.; Park, J.-K.; Ryou, M.-H.; Lee, Y. M. Stabilizing Effect of 2-(Triphenylphosphoranylidene) Succinic Anhydride as Electrolyte Additive on the Lithium Metal of Lithium Metal Secondary Batteries. *Electrochim. Acta* **2015**, *170*, 353−359.
(15) Grande, L.; von Zamory, J.; Koch, S. L.; Kalhoff, J.; Paillard, E.; Passerini, S. Homogeneous Lithium Electrodeposition with Pyrrolidinium-Based Ionic Liquid Electrolytes. *ACS Appl. Mater. Interfaces* **2015**, *7*, 5950−5958.
(16) Choi, S. M.; Kang, I. S.; Sun, Y. K.; Song, J. H.; Chung, S. M.; Kim, D. W. Cycling Characteristics of Lithium Metal Batteries Assembled with a Surface Modified Lithium Electrode. *J. Power Sources* **2013**, *244*, 363−368.
(17) Kang, I. S.; Lee, Y. S.; Kim, D. W. Improved Cycling Stability of Lithium Electrodes in Rechargeable Lithium Batteries. *J. Electrochem. Soc.* **2014**, *161*, A53−A57.
(18) Lee, H.; Lee, D. J.; Kim, Y. J.; Park, J. K.; Kim, H. T. A Simple Composite Protective Layer Coating That Enhances the Cycling Stability of Lithium Metal Batteries. *J. Power Sources* **2015**, *284*, 103−108.
(19) Tatsuma, T.; Taguchi, M.; Oyama, N. Inhibition Effect of Covalently Cross-Linked Gel Eelectrolytes on Lithium Dendrite Formation. *Electrochim. Acta* **2001**, *46*, 1201−1205.
(20) Lee, Y. S.; Lee, J. H.; Choi, J. A.; Yoon, W. Y.; Kim, D. W. Cycling Characteristics of Lithium Powder Polymer Batteries Assembled with Composite Gel Polymer Electrolytes and Lithium Powder Anode. *Adv. Funct. Mater.* **2013**, *23*, 1019−1027.

DOI: 10.1021/acsami.5b07730
ACS Appl. Mater. Interfaces 2015, 7, 23700−23707

(21) Khurana, R.; Schaefer, J. L.; Archer, L. A.; Coates, G. W. Suppression of Lithium Dendrite Growth Using Cross-Linked Polyethylene/Poly(ethylene oxide) Electrolytes: A New Approach for Practical Lithium-Metal Polymer Batteries. *J. Am. Chem. Soc.* **2014**, *136*, 7395−7402.
(22) Park, K.; Cho, J. H.; Shanmuganathan, K.; Song, J.; Peng, J.; Gobet, M.; Greenbaum, S.; Ellison, C. J.; Goodenough, J. B. New Battery Strategies with a Polymer/Al_2O_3 Separator. *J. Power Sources* **2014**, *263*, 52−58.
(23) Tu, Z.; Kambe, Y.; Lu, Y.; Archer, L. A. Nanoporous Polymer-Ceramic Composite Electrolytes for Lithium Metal Batteries. *Adv. Energy Mater.* **2014**, *4*, DOI: 10.1002/aenm.201300654.
(24) Wang, Z.; Guo, F.; Chen, C.; Shi, L.; Yuan, S.; Sun, L.; Zhu, J. Self-Assembly of PEI/SiO_2 on Polyethylene Separators for Li-Ion Batteries with Enhanced Rate Capability. *ACS Appl. Mater. Interfaces* **2015**, *7*, 3314−3322.
(25) Ryou, M. H.; Lee, Y. M.; Park, J. K.; Choi, J. W. Mussel-Inspired Polydopamine-Treated Polyethylene Separators for High-Power Li-Ion Batteries. *Adv. Mater.* **2011**, *23*, 3066−3070.
(26) Ryou, M. H.; Lee, D. J.; Lee, J. N.; Lee, Y. M.; Park, J. K.; Choi, J. W. Excellent Cycle Life of Lithium-Metal Anodes in Lithium-Ion Batteries with Mussel-Inspired Polydopamine-Coated Sseparators. *Adv. Energy Mater.* **2012**, *2*, 645−650.
(27) Yan, K.; Lee, H.-W.; Gao, T.; Zheng, G.; Yao, H.; Wang, H.; Lu, Z.; Zhou, Y.; Liang, Z.; Liu, Z.; Chu, S.; Cui, Y. Ultrathin Two-Dimensional Atomic Crystals as Stable Interfacial Layer for Improvement of Lithium Metal Anode. *Nano Lett.* **2014**, *14*, 6016−6022.
(28) Wang, X.; Sun, G.; Routh, P.; Kim, D. H.; Huang, W.; Chen, P. Heteroatom-Doped Graphene Materials: Syntheses, Properties and Applications. *Chem. Soc. Rev.* **2014**, *43*, 7067−7098.
(29) Zhu, J.; Yang, D.; Yin, Z.; Yan, Q.; Zhang, H. Graphene and Graphene-Based Materials for Energy Storage Applications. *Small* **2014**, *10*, 3480−3498.
(30) Jana, A.; Ely, D. R.; García, R. E. Dendrite-Separator Interactions in Lithium-Based Batteries. *J. Power Sources* **2015**, *275*, 912−921.
(31) Kannan, A. G.; Zhao, J.; Jo, S. G.; Kang, Y. S.; Kim, D. W. Nitrogen and Sulfur Co-Doped Graphene Counter Eelectrodes with Synergistically Enhanced Performance for Dye-Sensitized Solar Cells. *J. Mater. Chem. A* **2014**, *2*, 12232−12239.
(32) Kim, J. H.; Kannan, A. G.; Woo, H. S.; Jin, D. G.; Kim, W.; Ryu, K.; Kim, D. W. A Bi-Functional Metal-Free Catalyst Composed of Dual-Doped Graphene and Mesoporous Carbon for Rechargeable Lithium-Oxygen Batteries. *J. Mater. Chem. A* **2015**, *3*, 18456−18465.
(33) Dong, Y.; Pang, H.; Yang, H. B.; Guo, C.; Shao, J.; Chi, Y.; Li, C. M.; Yu, T. Carbon-Based Dots Co-doped with Nitrogen and Sulfur for High Quantum Yield and Excitation-Independent Emission. *Angew. Chem., Int. Ed.* **2013**, *52*, 7800−7804.
(34) Ding, W.; Wei, Z.; Chen, S.; Qi, X.; Yang, T.; Hu, J.; Wang, D.; Wan, L.-J.; Alvi, S. F.; Li, L. Space-Confinement-Induced Synthesis of Pyridinic- and Pyrrolic-Nitrogen-Doped Graphene for the Catalysis of Oxygen Reduction. *Angew. Chem., Int. Ed.* **2013**, *52*, 11755−11759.
(35) Paraknowitsch, J. P.; Thomas, A.; Schmidt, J. Microporous Sulfur-Doped Carbon from Thienyl-Based Polymer Network Precursors. *Chem. Commun.* **2011**, *47*, 8283−8285.
(36) Kudin, K. N.; Ozbas, B.; Schniepp, H. C.; Prud'homme, R. K.; Aksay, I. A.; Car, R. Raman Spectra of Graphite Oxide and Functionalized Graphene Sheets. *Nano Lett.* **2007**, *8*, 36−41.
(37) Li, X.; Wang, H.; Robinson, J. T.; Sanchez, H.; Diankov, G.; Dai, H. Simultaneous Nitrogen Doping and Reduction of Graphene Oxide. *J. Am. Chem. Soc.* **2009**, *131*, 15939−15944.
(38) Naylor, C. C.; Meier, R. J.; Kip, B. J.; Williams, K. P. J.; Mason, S. M.; Conroy, N.; Gerrard, D. L. Raman Spectroscopy Employed for the Determination of the Intermediate Phase in Polyethylene. *Macromolecules* **1995**, *28*, 2969−2978.
(39) Ferrari, A. C.; Meyer, J. C.; Scardaci, V.; Casiraghi, C.; Lazzeri, M.; Mauri, F.; Piscanec, S.; Jiang, D.; Novoselov, K. S.; Roth, S.; Geim, A. K. Raman Spectrum of Graphene and Graphene Layers. *Phys. Rev. Lett.* **2006**, *97*, 187401.
(40) Garaj, S.; Hubbard, W.; Reina, A.; Kong, J.; Branton, D.; Golovchenko, J. A. Graphene as a Sub-Nanometer Trans-Electrode Membrane. *Nature* **2010**, *467*, 190−193.
(41) Itagaki, M.; Kobari, N.; Yotsuda, S.; Watanabe, K.; Kinoshita, S.; Ue, M. $LiCoO_2$ Electrode/Electrolyte Interface of Li-Ion Rechargeable Batteries Investigated by In Situ Electrochemical Impedance Spectroscopy. *J. Power Sources* **2005**, *148*, 78−84.

DOI: 10.1021/acsami.5b07730
ACS Appl. Mater. Interfaces 2015, 7, 23700−23707